

OPEN

Tunable three-way topological energy-splitter

Mehul P. Makwana^{1,2*} & Gregory Chaplain¹

Strategically combining four structured domains creates the first ever three-way topological energy-splitter; remarkably, this is only possible using a square, or rectangular, lattice, and not the graphene-like structures more commonly used in valleytronics. To achieve this effect, the two mirror symmetries, present within all fully-symmetric square structures, are broken; this leads to two nondistinct interfaces upon which valley-Hall states reside. These interfaces are related to each other via the time-reversal operator and it is this subtlety that allows us to ignite the third outgoing lead. The geometrical construction of our structured medium allows for the three-way splitter to be adiabatically converted into a wave steerer around sharp bends. Due to the tunability of the energies directionality by geometry, our results have far-reaching implications for applications such as beam-splitters, switches and filters across wave physics.

A fundamental understanding of the manipulation and channeling of wave energy underpins advances in device design in acoustics and optics^{1–3}. For instance, beam-splitters, that split an incident beam of light in two, are extensively used for experiments and devices in quantum computing, astrophysics, relativity theory and other areas of physics^{4,5}. This desire to guide waves, split and redirect them, for broadband frequencies, in a lossless and robust manner, extends well beyond optical devices and into electromagnetism, vibration control and acoustic switches, amongst other fields^{6–8}. Fortunately, the advent of topological insulators in quantum mechanics^{9,10}, and their translation into classical systems, has led to waveguides that are more broadband and robust than previous designs^{11–15} and ultimately to robust networks^{16–20}; however, the vast majority of the topological energy-splitters are based upon graphene-like hexagonal structures and hence restricted to a two-way partitioning of energy. Herein we rectify this with an intelligently engineered three-way topological energy-splitter, the geometrical design of which is based upon the square lattice^{21,22}.

Time-reversal symmetric (TRS) topological guides leverage the discrete valley degrees of freedom that arise from degenerate extrema in Fourier space. When constructing topological guides, graphene-like materials are the prime candidate due to their well-defined KK' valleys; these valleys are distinguished by their opposite chirality and related by TRS. The intervalley scattering is heavily suppressed^{23–26} by the large Fourier separation between the two valleys, and each valley becomes an efficient information carrier. These valley modes are attracting growing attention, in part due to their simplicity of construction, leading to the emergent field of valleytronics^{10–15}. The primary benefits of these topologically nontrivial modes over, cavity and topologically trivial interfacial modes²⁶, is the additional topological protection afforded by the chiral flux either side of the zero-line modes (ZLMs) and geometrical tunability²⁶ allowing a bend to be adiabatically converted into a splitter (and vice-versa).

The prevalence of graphene-like structures has primarily limited valleytronic devices to *two-way* energy-splitters; this is motivated by the conservation of chirality at the KK' valleys^{16–20,27–39}. A three-way and a four-way partitioning of energy away from a nodal *region* was shown in⁴⁰ and²⁶, respectively, however the latter was dependent upon the tunneling mechanism whilst the former was for a multilayer system. Tunneling would introduce an additional dependency upon the system; namely, the decay length perpendicular to the direction of propagation. Hence, the transmission along the outgoing leads would be heavily contingent upon the location of the mode within the topologically nontrivial band-gap; therefore an alternative method whereby the energy is partitioned away from a well-defined nodal *point* as opposed to a nodal *region* is highly desirable. Importantly, this is only possible using a square or rectangular lattice; the three-way energy splitting is dependent upon the equivalence of the interfaces (modulo time-reversal symmetry) that is only achievable using the four-fold symmetric cellular structure. The *geometrical tunability*, the *topological robustness* and the *three-way* partitioning of energy away from a well-defined nodal *point* are three crucial advantages of the square energy-splitter (see Fig. 1) over competing designs.

¹Department of Mathematics, Imperial College London, London, SW7 2AZ, UK. ²Multiwave Technologies AG, 3 Chemin du Prê Fleuri, 1228, Geneva, Switzerland. *email: mehul.makwana07@imperial.ac.uk

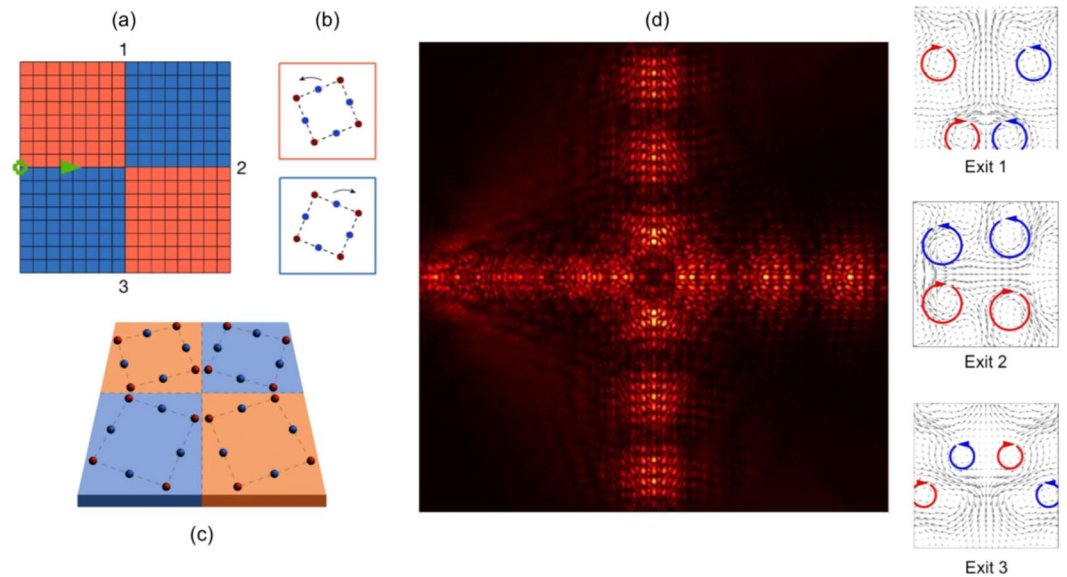


Figure 1. Three-way topological splitter ($\omega = 6.5356$) — (a,b) The canonical splitter geometry of four structured quadrants. Different orientation of scatterers in the orange and blue regions. Source is indicated by circle at left edge. (c) Zoom-in of nodal region cells. (d) Displacement field, illustrating the splitting of energy three ways, panels on right illustrate the opposite chirality at the interfaces.

We begin in Sec. 2 by explicitly recasting the continuum plate model into the language of quantum mechanics, utilising a Hamiltonian description, while retaining elements of the continuum language to bridge across the quantum and elastic plate communities. Despite us utilising the structured elastic plate equation, our theories are system independent, hence are transposable to other classical systems. We examine a square cellular structure containing only a single mirror symmetry in Sec. 3; we demonstrate how this restricts a medium, comprised of these cells, to solely yield straight valley-Hall guides i.e. the energy cannot be navigated around a bend. Contrastingly, the structure examined in Sec. 4 contains two mirror symmetries which in turn allows for ZLMs to couple around a bend as well as partition three-ways away from a nodal point. A few concluding remarks are drawn together in Sec. 5.

Results

Formulation. The group theoretic and topological concepts foundational to our approach hold irrespective of any specific two-dimensional scalar wave system. We choose to illustrate them here using a structured thin elastic Kirchhoff- Love (K-L) plate⁴¹ for which many results for point scatterers are explicitly available⁴²; the geometrical ideas themselves carry across to photonics, phononics and plasmonics. Displacement Bloch eigenstates $|\psi_{n\kappa}\rangle$ satisfy the (non-dimensionalised) K-L equation,

$$\begin{aligned} \hat{H}|\psi_{n\kappa}\rangle &= \omega_{n\kappa}^2|\psi_{n\kappa}\rangle + F(\mathbf{x})|\psi_{n\kappa}\rangle, \\ \hat{H} &= \int |\mathbf{x}\rangle\delta(\mathbf{x} - \mathbf{y})\nabla_{\mathbf{x}}^4\langle\mathbf{y}|dx dy, \\ F(\mathbf{x}) &= \omega_{n\kappa}^2 \sum_1^P \sum_{p=1}^P M_1^{(p)}\psi_{n\kappa}^{(p)}(\mathbf{x})\delta(\mathbf{x} - \mathbf{x}_1^{(p)}), \end{aligned} \tag{1}$$

for Bloch-wavevector κ , n denoting the eigenmodes and $\omega_{n,\kappa}$ the non-dimensionalised frequency; reaction forces at the point constraints, $F(\mathbf{x})$, introduce dependence upon the direct lattice. The most straightforward constraints, sufficient for our purposes, are point mass-loading $F(\mathbf{x})$ with the reaction forces proportional to the displacement via an effective impedance coefficient. Here 1 labels each elementary cell that repeats periodically to create the infinite physical plate crystal, and each cell contains $p = 1 \dots P$ constraints. In an infinite medium the displacements are Bloch eigenfunctions

$$\psi_{n\kappa}(\mathbf{x}) = \langle\mathbf{x}|\psi_{n\kappa}\rangle = \exp(i\kappa \cdot \mathbf{x})\langle\mathbf{x}|u_{n\kappa}\rangle, \tag{2}$$

where $|u_{n\kappa}\rangle$ is a periodic eigenstate. The displacements satisfy the following completeness and orthogonality relations:

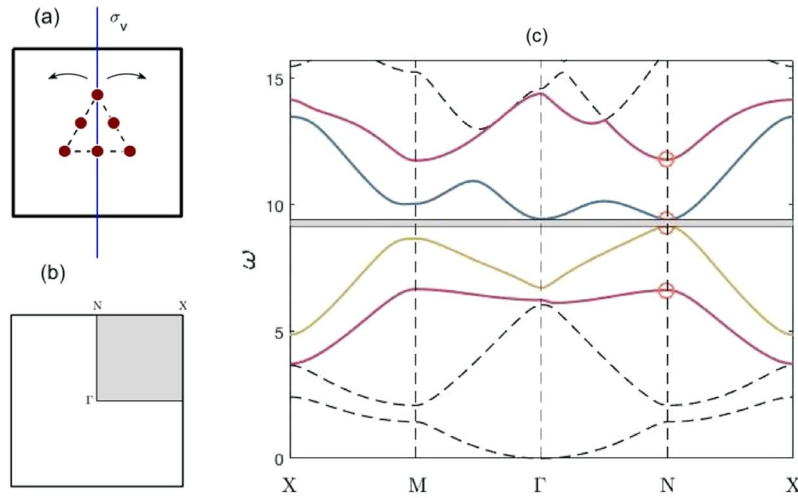


Figure 2. (a) Cellular structure shown; uniform mass values of 1, lattice constant of 2, centroid to vertex mass distance of 0.45. Pre-perturbation structure has σ_v symmetry, post-perturbation structure breaks σ_v symmetry via an angular perturbation of the inclusion set. (b) Shows the irreducible Brillouin zone (IBZ, shaded region) within the Brillouin zone (BZ). (c) Dispersion curves C_{2v} case (when $\omega_{A_1} > \omega_{B_1}$ at N) — Parameter values are different to those in Fig. 2; σ_v symmetry present within physical space cell. Parameter values: distance between centroid and vertex mass = 0.45, lattice constant = 2, vertex mass value = 1, non-vertex mass value = 0.5. The coloured bands are associated with the SSE. In this instance, A_1 curve lies above B_1 curve at N , hence there is no band crossing along NX .

$$\begin{aligned} \sum_{n\kappa} |\psi_{n\kappa}\rangle \langle \psi_{n\kappa}| &= \hat{1}, \\ \langle \psi_{n\kappa} | \psi_{m\kappa'} \rangle &= \delta_{nm} \delta_{\kappa, \kappa'}, \\ \int u_{n\kappa}^* u_{m\kappa'} \exp(i\Delta\kappa' \cdot \mathbf{x}) d\mathbf{x} &= \delta_{nm} \delta_{\kappa, \kappa'}, \end{aligned} \tag{3}$$

where $\Delta\kappa' = \kappa' - \kappa$. Due to the completeness of the periodic eigensolution, we can expand $|u_{n\kappa}\rangle$ in the complete orthogonal basis set $\{u_{j\kappa_0}(\mathbf{x})\}$ where κ_0 is fixed,

$$\begin{aligned} |\psi_{n\kappa}\rangle &= \exp(i\kappa \cdot \mathbf{x}) |u_{n\kappa}\rangle \\ &= \exp(i\kappa \cdot \mathbf{x}) \sum_m A_{nm}(\kappa) |u_{m\kappa_0}\rangle \\ &= \exp(i\Delta\kappa \cdot \mathbf{x}) \sum_m A_{nm}(\kappa) |\psi_{m\kappa_0}\rangle, \end{aligned} \tag{4}$$

where $\Delta\kappa = \kappa - \kappa_0$. After substituting (4), into the governing Eq. (1), we explicitly obtain,

$$\begin{aligned} \exp(i\Delta\kappa \cdot \mathbf{x}) \sum_m A_{nm}(\kappa) [(\omega_{m\kappa_0}^2 - \omega_{n\kappa}^2) \mathbf{1} + \sum_{\mathbf{N}, p} M_N^{(p)} \delta(\mathbf{x} - \mathbf{x}_N^{(p)})] \\ + 4i\Delta\kappa \cdot \nabla_{\mathbf{x}}^3 + \mathcal{O}(|\Delta\kappa|^2) |\psi_{j\kappa_0}(\mathbf{x}) = 0. \end{aligned} \tag{5}$$

up to first-order in $|\Delta\kappa|$. This expansion will be used in the subsequent section, alongside symmetry considerations, to engineer the Dirac cones. A categorisation of planar structures that yield non-symmetry induced Dirac cones was shown in⁴³.

C_{2v} cellular structure. In this section we examine the cellular structure shown in Fig. 2(a). Spatially, this structure solely has σ_v reflectional symmetry; however, in Fourier space, it has C_{2v} symmetry, due to the presence of time-reversal symmetry. In subsection 3.1, we utilise the expansion (5) and group theoretical considerations to demonstrate how an accidental Dirac cone is engineered. The effects of σ_v symmetry breaking, on the bulk bandstructure, are discussed in subsection 3.2. Subsection 3.3 demonstrates how the strategic stacking of geometrically distinct media results in valley-Hall edge states^{10,15}. A ZLM connected to a valley-Hall edge state is shown in subsection 3.4 alongside a justification for why this particular C_{2v} model does not allow for propagation around corners. Since the valley-Hall state is a weak topological state protected solely by symmetry, care must be taken to prohibit backscattering hence knowledge of the long-scale envelope is especially useful for finite length interfaces as it can be used to minimise the backscattering. An asymptotic method, more commonly known as high-frequency

Classes → IR ↓	E	C_2	σ_v	σ_h	Basis functions
A_1	+1	+1	+1	+1	x^2, y^2
A_2	+1	+1	-1	-1	xy
B_1	+1	-1	+1	-1	x, xy^2
B_2	+1	-1	-1	+1	y, x^2y

Table 1. C_{2v} character table.

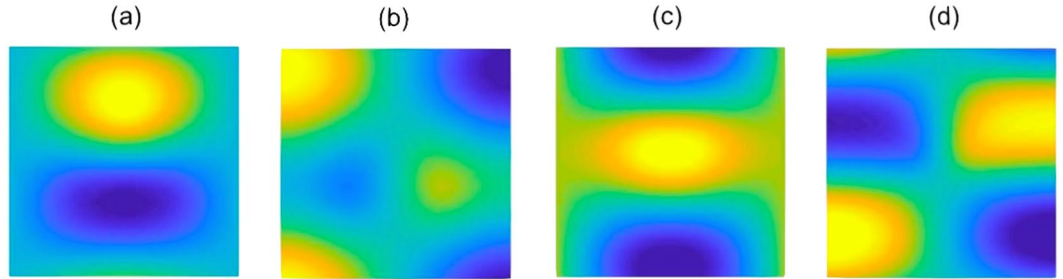


Figure 3. Eigensolutions, at N , for C_{2v} case with σ_v symmetry. Panel (a), IR: B_2 , Basis: y . Panel (b), IR: B_1 , Basis: x . Panel (c), IR: A_1 , Basis: x^2, y^2 . Panel (d), IR: A_2 , Basis: xy .

homogenisation (HFH) allows for the characterisation of this long-scale envelope (see Methods); this is applied to a C_{2v} ZLM in subsection 3.4.

Engineering an accidental Dirac cone. Band coupling at high-symmetry point for C_{2v} structure. The point group symmetry of the structure, shown in Fig. 2(a), is $G_\Gamma = C_{2v}$; this is also the point group symmetry at N , $G_N = C_{2v}$ (Table 1). The C_{2v} point group arises from a combination of spatial (reflectional) and time-reversal symmetries; the latter relates $\kappa \rightarrow -\kappa$. The group theoretical arguments used throughout this subsection, are reminiscent of those found in²¹ although in our calculations we have applied an actual asymptotic scheme whereby we have judiciously chosen a small parameter with a distinguished limit.

The irreducible representations (IRs) at N are one-dimensional hence there is no symmetry induced degeneracy. Despite this, we shall demonstrate in this subsection how two of the IRs can be tuned such that an accidental degeneracy (that is not symmetry repelled) forms. The four solid bands in Fig. 2(c) (bands numbered 3–6 inclusive) are associated with the eigensolutions, shown in Fig. 3, these match the basis function symmetries of the C_{2v} group (Table 1); hence this indicates that bands 3–6 are symmetry induced and the sequential ordering of them (lowest to highest) is deduced numerically, via the eigensolutions, as: $\{B_2, A_1, B_1, A_2\}$.

It is expected, from the dispersion curves (Fig. 2(c)) that the two bands that form the accidental degeneracy, namely A_1, B_1 , have a strong influence on each other whilst the other two symmetry induced bands, B_2, A_2 , will have a limited effect on the local curvature or slope of the A_1, B_1 bands⁴⁴; the effect, by the bands that lie outside of bands 3–6, on the A_1, B_1 bands, is expected to be negligible; to see these points mathematically we initially separate out the eigenket expansion Eq. (4) into two sets of bands; namely, the symmetry set eigensolutions (SSE), bands 3–6, and those that lie outside the SSE,

$$|\psi_{n\kappa}\rangle = \exp(i\Delta\kappa \cdot \mathbf{x}) \left[\sum_{j \in \text{SSE}} A_{nj}(\kappa) |\psi_{j\kappa_0}\rangle + \sum_{\alpha \notin \text{SSE}} A_{n\alpha}(\kappa) |\psi_{\alpha\kappa_0}\rangle \right]. \tag{6}$$

Motivated by the orthogonality condition (3) and the expansion (6), we multiply Eq. (4), by $\psi_{l\kappa_0}^*(\mathbf{x})$ or $\psi_{\beta\kappa_0}^*(\mathbf{x})$ (where $l \in \text{SSE}, \beta \notin \text{SSE}$) before integrating over the primitive cell to obtain the following two equations,

$$\begin{aligned} (\omega_{n\kappa}^2 - \omega_{l\kappa_0}^2) \Lambda_l A_{nl} &= \sum_j H_{lj} A_{nj} + \sum_\alpha H_{l\alpha} A_{n\alpha}, \\ (\omega_{n\kappa}^2 - \omega_{\beta\kappa_0}^2) A_{n\beta} &= \sum_j H'_{\beta j} A_{nj} + \sum_\alpha H'_{\beta\alpha} A_{n\alpha} \end{aligned} \tag{7}$$

where the κ dependence of the weighting coefficients has been dropped; $\Lambda_l, H_{ab}, H'_{ab}$ are explicitly,

$$\begin{aligned} \Lambda_l &= 1 + \sum_p M_l^{(p)} \left| \psi_{l\kappa_0}(\mathbf{x}_1^{(p)}) \right|^2, \\ H_{ab} &= \Delta\kappa \cdot \langle \psi_{a\kappa_0} | 4i \nabla_{\mathbf{x}} | \psi_{b\kappa_0} \rangle + \mathcal{O}(|\Delta\kappa|^2), \end{aligned} \tag{8}$$

$$H'_{ab} = H_{ab} + \delta_{ab}(\omega_{n\kappa}^2 - \omega_{b\kappa_0}^2) \sum_p M_{\Gamma}^{(p)} \psi_{a\kappa_0}^*(x_{\Gamma}^{(p)}) \psi_{b\kappa_0}(x_{\Gamma}^{(p)}) + \mathcal{O}(|\Delta\kappa|^2). \quad (9)$$

Rearranging the second equation in (7) to,

$$A_{n\beta} = \frac{\sum_j H_{j\beta} A_{nj} + \sum_{\alpha} H'_{\beta\alpha} A_{n\alpha}}{(\omega_{n\kappa}^2 - \omega_{\beta\kappa_0}^2)} \quad (10)$$

and substituting this into the second summation of the first equation gives,

$$(\omega_{n\kappa}^2 - \omega_{l\kappa_0}^2) \Lambda_l A_{nl} = \sum_j H_{lj} A_{nj} + \sum_j A_{nj} \sum_{\alpha} \frac{H_{l\alpha} H_{\alpha j}}{(\omega_{n\kappa}^2 - \omega_{\alpha\kappa_0}^2)}, \quad (11)$$

where we have neglected terms which couple states outside the SSE to other states outside the SSE. If we let $n = l \in \text{SSE}$ and $\kappa = \kappa_0 + \Delta\kappa$ then the frequency term on the left-hand side is expanded to yield,

$$\omega_{n\kappa}^2 = \omega_{l\kappa_0}^2 + 2\omega_{l\kappa_0} \Delta\kappa \cdot \nabla_{\kappa} \omega_{l\kappa_0} + \mathcal{O}(|\Delta\kappa|^2). \quad (12)$$

Hence, from this expansion it is easy to see that the second summation in (11), that couples states within the SSE to those outside, falls into second-order hence the effective first-order equation is,

$$(2\omega_{l\kappa_0} \Delta\omega_l \Lambda_l) A_{nl} = \sum_{j \in \text{SSE}} H_{lj} A_{nj}, \quad (13)$$

where $\Delta\omega_l = \omega_{l\kappa} - \omega_{l\kappa_0}$ and $l \in \text{SSE}$. Notably, the higher-order corrections, that encompass the coupling between bands within the SSE to those outside, provide the band curvature details away from a locally linear point. In this instance, Eq. (13) is a 4×4 matrix eigenvalue problem, where the Hamiltonian, with components H_{lj} , is Hermitian. If, for a particular κ_0 , the first-order term is zero we would have to proceed to second-order; here additional terms would come from the fourth-ordered derivative, the $\omega_{l\kappa}$ expansion and band coupling between outside SSE and inside SSE bands.

Compatibility relations and band tunability along NX . Bands tend to vary continuously except possibly at accidental degeneracies where modal inversion may occur which in turn leads to a discontinuity of the intersecting surfaces. Hence, the eigenfunctions continuously transform as you progress along a continuous IBZ path of simple eigenvalues. The associated IRs, that describe the transformation properties of the eigenfunctions, themselves smoothly transition into IRs that belong to the point groups along $N\Gamma$ or NX .

In physical space the cellular structure only has σ_v spatial symmetry, this is equivalent to σ_h symmetry in Fourier space, Fig. 4(b). Recall the definition of a point group symmetry, i.e. any symmetry operator $\hat{R} \in G_{\Gamma}$ that satisfies, $\hat{R}\kappa = \kappa \bmod \mathbf{G}$, where \mathbf{G} is a reciprocal lattice basis vector; this implies that $\kappa \in NX$ solely has the mirror symmetry operator, σ_h within its point group. Similarly, for a $\kappa \in \Gamma N$, only the vertical mirror symmetry operator, $\sigma_v \in C_{2v}$, satisfies the point group criterion. The symmetries of the eigenfunctions, for a κ belonging to either of the paths, NX and $N\Gamma$, are shown within the basis functions column of the $\sigma_{v,h}$ Table 2. If we solely consider the two strongly coupled bands, represented by the IRs A_1 and B_1 , then the associated eigenfunctions transitional behaviour, away from N , is described by the $\sigma_{v,h}$ character table. Due to the continuity of the bands the A_1, B_1 IRs belonging to the C_{2v} table will transform into the IRs, of the $\sigma_{v,h}$ table, as we move away from N ; the relationships between different IRs are more commonly referred to as compatibility relations^{44,45}. Initially, we consider symmetry σ_h , the eigenstates at N and along NX satisfy the following,

$$\hat{P}_{\sigma_h} |\psi_{A_1, B_1}\rangle = \pm |\psi_{A_1, B_1}\rangle, \quad \hat{P}_{\sigma_h} |\psi_{A, B}\rangle = \pm |\psi_{A, B}\rangle. \quad (14)$$

Hence, the bands (A_1, B_1) (at N) are compatible with (A, B) (along NX). Physically, this transition is also evident from the eigensolutions; as $B_1 \rightarrow B$ the eigensolution may also satisfy oddness relative to the x -axis (see Fig. 3). Similarly, at N and along $N\Gamma$, the eigenstates transform under σ_v as,

$$\hat{P}_{\sigma_v} |\psi_{A_1, B_1}\rangle = \pm |\psi_{A_1, B_1}\rangle, \quad \hat{P}_{\sigma_v} |\psi_{A, B}\rangle = + |\psi_{A, B}\rangle. \quad (15)$$

This implies that the bands (A_1, B_1) (at N) are compatible with (A, A) (along $N\Gamma$). These compatibility relations are summarised pictorially in the unfurled IBZ path (Fig. 4(c)). Importantly, note that, in deriving Eq. (13) we have only assumed that κ_0 belongs to a particular symmetry set band (surfaces 3–6) (the band at κ_0 must be continuously connected to the same band at N). Therefore, the compatibility relations allow us to choose any expansion point along the the path ΓNX where the eigenfunction basis set, Eq. (4), transforms accordingly i.e. $|\psi_{A_1}\rangle \rightarrow |\psi_A\rangle$.

In order to solve the 2-band eigenvalue problem, Eq. (13), we compute the determinant of the truncated matrix,

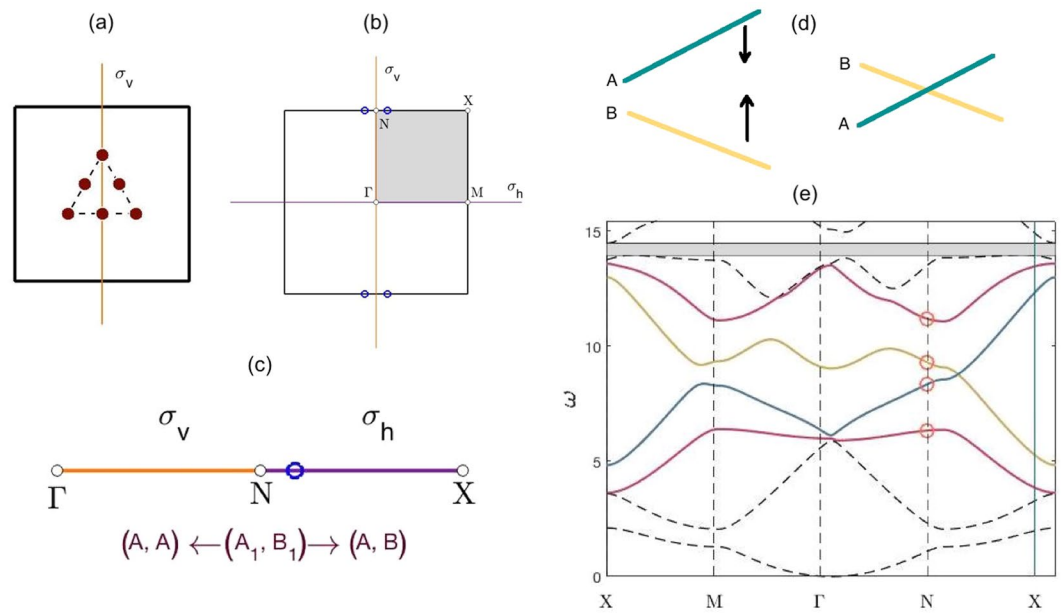


Figure 4. Physical and Fourier space cells — (a) Cellular structure in physical space. (b) IBZ (shaded region) shown within BZ. Presence of σ_v symmetry in physical space translates into σ_h symmetry in Fourier space, this explains the symmetrical placement of the Dirac cones (blue circles) either side of σ_h . (c) Unfurled IBZ path. Symmetries and IRs, along the paths $\Gamma \rightarrow N \rightarrow X$, are shown. Panel (d) Effect of parametric tuning on A, B bands — When B curve lies about the A curve, the parameters denoted by $\Lambda_{A,B}$ can be altered to change the intersection location. For our model, the number of masses, their location (σ_v symmetry preserved) and their mass values can all be varied. Panel (e) Dispersion curves C_{2v} case (when $\omega_{B_1} > \omega_{A_1}$ at N) — Parameter values same as those in Fig. 2; σ_v symmetry present within physical space cell. In this instance, B_1 curve lies above A_1 curve at N , hence there is band crossing along NX .

Classes → IR ↓	σ_h	σ_v	Basis functions
A_1	+1	+1	x^2, y^2, xy
B_1	-1	+1	x, xy^2
Classes → IR ↓	E	σ_{vh}	Basis functions
A	+1	+1	x^2, y^2, xy
B	+1	-1	x, y, x^2y, xy^2

Table 2. σ_{vh} character table and selected portion of C_{2v} character table.

$$\begin{vmatrix} -2\omega_A \Delta\omega_A \Lambda_A & \Delta\kappa_x \langle \psi_A | \partial_x^3 + \partial_x \partial_y^2 | \psi_B \rangle \\ \Delta\kappa_x \langle \psi_A | \partial_x^3 + \partial_x \partial_y^2 | \psi_B \rangle^* & -2\omega_B \Delta\omega_B \Lambda_B \end{vmatrix} = 0,$$

where parity considerations^{44,45} allows for simplification of the Hermitian matrix; the eigensolutions are evaluated at κ_0 . Solving the eigenvalue problem yields the following result,

$$2\omega_{A,B} \Delta\omega_{A,B} \Lambda_{A,B} = \pm \Delta\kappa_x \langle \psi_A | \partial_x^3 + \partial_x \partial_y^2 | \psi_B \rangle, \tag{16}$$

where the \pm corresponds to the A, B bands, respectively. This result implies that the A, B bands have an identical slope, albeit with opposite gradients; hence, if, at N an instance can be found where $\omega_{B_1} > \omega_{A_1}$ then the bands will invariably cross along the path NX . The parametric variation afforded to us, and encompassed in the variable $\Lambda_{A,B}$, merely increases or decreases the slope thereby increasing or decreasing the distance between N and the Dirac point. Note that the Dirac cone occurs along the spatial symmetry path, σ_h , of the structure due to the opposite parities of the A, B bands; band repulsion occurs along the $N\Gamma$ path²² thereby resulting in a partial band gap along $N\Gamma$. If $\omega_{B_1} > \omega_{A_1}$, then the partial gap along $N\Gamma$ isolates the Dirac cone along a portion of the IBZ path, ΓNX .

The distance between the Dirac and high-symmetry point is highly relevant for the transmission properties of the topological guide²⁶ stated that the transmission is better for short wave envelopes, as opposed to long wave

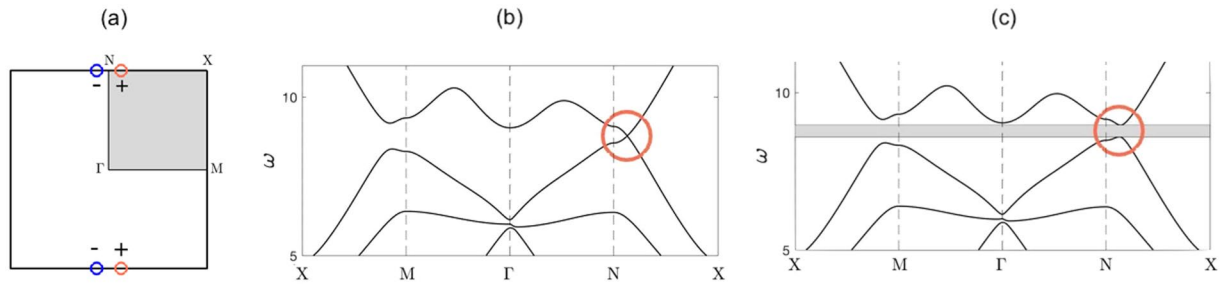


Figure 5. (a) IBZ (shaded region) within the Brillouin zone (BZ); circles indicate Dirac cone locations pre-perturbation, whilst \pm denotes the signum of the post-perturbation C_v . Dirac cones solely along single set of parallel HSLs, not both. Dispersion curves for the C_{2v} case. Panel (b) pre-perturbation curves, when structure in Fig. 2(a) possesses σ_v symmetry. Rotation of inclusion set in Fig. 2(a) removes σ_v symmetry and yields the post-perturbation curves shown in panel (c).

envelopes, hence, for transmission post the nodal region, it is desirable to increase the distance between the Dirac cone and N . The latter is true due to the connection between the bulk and projected bandstructures⁴⁶, the bulk BZ is reduced to a one-dimensional BZ because the only relevant wavevector component for a straight guide is the one parallel to the ZLM. All wavevectors are projected onto the ΓM line in Fourier space, hence if the distance between N and the Dirac cone is increased then the Fourier separation between oppositely propagating modes, along the topological guide, would be increased. A mechanism to do this would be by altering the system parameters; Fig. 4(d,e) and Eq. (16) demonstrate that the slopes of the A and B bands can be increased or decreased by the system parameters thereby altering the position of the band intersection.

Breaking σ_v symmetry. From the previous subsection we know that when the σ_v symmetry is preserved an accidental Dirac degeneracy can be created; the bands coalescing along NX in Fig. 5(b) are parametrically engineered to do so. An important nuance is that the Dirac points are solely located along the two high-symmetry lines (HSLs), parallel to σ_h , and not along the perpendicular HSLs (see Fig. 4(b)); this is critical when it comes to energy-splitting. The σ_v symmetry is lost in Fourier space when the internal set of inclusions is rotated and this breaks open the Dirac point to create a band-gap, Fig. 5(c). The locally quadratic curves, in the vicinity of the former Dirac cones, are commonly referred to as “valleys” and they carry nonzero valley Chern numbers (Fig. 5(a)) which in turn leads to the generation of valley-Hall edge modes^{47,48}. The valley Chern number (C_v) is formally defined as follows,

$$\begin{aligned}
 C_v &= \frac{1}{2\pi} \int_S \nabla_\kappa \times i \langle \psi_{n\kappa} | \nabla_x | \psi_{n\kappa} \rangle d\kappa \\
 &= \frac{i}{2\pi} \oint_\gamma \langle \psi_{n\kappa} | \nabla_x | \psi_{n\kappa} \rangle \cdot d\mathbf{l} \\
 &= \frac{i}{2\pi} \oint_\gamma \sum_j A_{nj}^*(\kappa) \nabla_\kappa A_{nj}(\kappa) \cdot d\mathbf{l} = \frac{\varphi}{2\pi},
 \end{aligned}
 \tag{17}$$

where the surface and line integrals are computed in the vicinity of the valleys, φ denotes the Berry phase and the Kohn-Luttinger coefficients, $A_{nj}(\kappa)$, are derived from a variation of Eq. (13) that contains the perturbation terms¹⁵. Both, C_v and φ are dependent upon the perturbation strength and hence are not quantized quantities. Despite this, a topological integer, $\text{sgn}(C_v)$, exists that yields a bulk-boundary correspondence valid for specific interfaces⁴⁹. These interfaces must ensure that regions of opposite $\text{sgn}(C_v)$ are not projected onto the same point in Fourier space; hence for the C_{2v} case, from Fig. 5(a), it is evident that an interface associated with the ΓM direction will lead to well-defined topological integers. In the next subsection, we shall show how, the locations of nonzero C_v , dictates how the geometrically distinct media are stacked.

C_{2v} adjoining ribbons. Attaching two topological media, with opposite $\text{sgn}(C_v)$ yields broadband chiral edge states¹⁰. This is achieved by placing one gapped medium, above its σ_v reflected twin; in essence, the stacking in Fourier space results in regions of opposite $\text{sgn}(C_v)$ overlaying each other, this local disparity ensures the presence of valley-Hall edge modes. The two distinct orderings of the media create two distinct interfaces, as seen in Fig. 6(a) one of which supports only the even modes and the other only the odd modes. This evenness and oddness of the edge modes is inherited from the even and odd bulk modes, Fig. 3. The *gapless* curves are a symptom of the topologically nontrivial nature of the edge states; this is akin to the valley-Hall modes seen for the zigzag interface within hexagonal structures.

The simplicity of this construction, the apriori knowledge of how to tessellate the two media to produce these broadband edge states, and the added robustness²⁶ are the main benefits of these topological valley-Hall modes. The additional functionality of having a three-way topological splitter (Fig. 1) comes with a caveat: The Fourier separation between the valleys controls the intervalley scattering and the smaller separation in the square lattice,

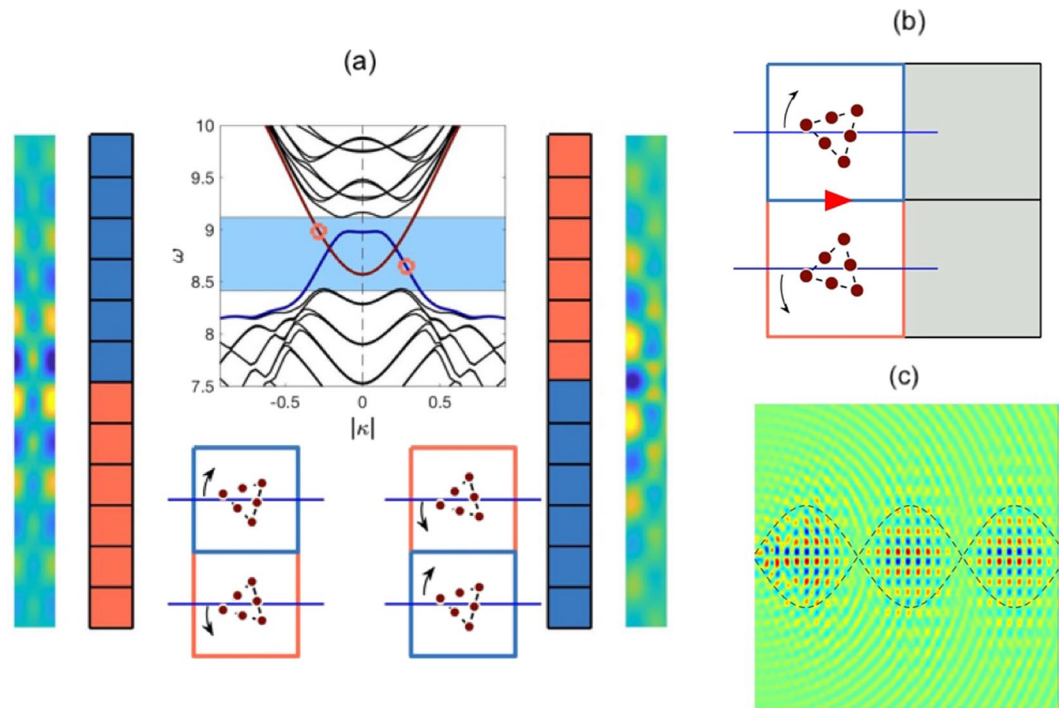


Figure 6. (a) Interfacial dispersion curves and ZLMs — *Top*: maroon curve arises when blue medium stacked over orange (left-sided ribbons), whilst navy curves, when orange over blue (right-sided ribbons). *Left*: even-parity ZLM, $\omega = 9.00$. *Right*: odd-parity ZLM, $\omega = 8.60$. (b) Odd-parity mode along blue over orange interface; importantly, there is no arrangement for the grey cells that ensures a vertical mode. As there are no well-defined valleys of nonzero C_v along the vertical edges of the BZ in Fig. 5, energy cannot be steered around a $\pi/2$ bend. (c) Dipolar source placed at leftmost edge, excites odd-parity ZLM. The periodicity of the long-scale envelope is clearly evident; outline around envelope derived from HFH (Methods). Backscattering can be minimised via parametric variation (by decreasing the wavelength of the energy-carrying envelope).

Fig. 6(a), vis-a-vis that for graphene-like structures²⁶ leads to increased scattering. This can be mitigated as the Fourier separation can be artificially increased by parametrically increasing the distance between the Dirac cone and N in Fig. 5(b) thereby acting to increase the robustness of the edge states against shorter-range defects.

C_{2v} ZLM and absence of post-bend propagation. The property of the C_{2v} case that prohibits propagation around the bend is the absence of well-defined valleys with nonzero C_v , along the vertical HSLs of the BZ, see Fig. 5(a). Hence, there is no arrangement that can be placed to the right of either stacking in Fig. 6(a) to obtain a ZLM perpendicular to the blue-orange interface, Fig. 6(b). The ZLM, Fig. 6(c), has a long-scale periodic envelope that can be captured using an effective medium theory⁵⁰ (see Methods). Knowledge of the long-scale envelope is especially useful for these finite length interfaces as it can be used to minimise the backscattering as one has, in effect, a Fabry-Pérot resonator.

To summarise, for this C_{2v} case, there are ZLMs along straight interfaces, however the energy cannot navigate around a $\pi/2$ bend because there is no post-bend mode to couple with.

C_{4v} cellular structure. We now extend the concepts illustrated in Sec. 3 to a cellular structure that possesses C_{4v} point group symmetry at Γ (see Fig. 7(a)). Due to this structure possessing two perpendicular mirror symmetries, as opposed to one, there exists regions of nonzero C_v along both edges of the square BZ, subsection 4.1 (Fig. 7(b)); this will be shown to yield propagation around a corner (subsection 4.2) as well as a three-way splitting of energy (subsection 4.3). An extensive comparison between the square structures, discussed within this article, and the earlier valleytronics models based upon graphene-like structures^{16–20,26–39} will be pictorially shown at the end of subsection 4.3.

Breaking σ_{vh} symmetries. The C_{4v} case, Fig. 7(a), is reminiscent of the C_{2v} case but now with the addition of σ_h symmetry in physical space. This reflectional symmetry yields additional Dirac cones along a parallel set of HSLs, perpendicular to those connected with the σ_v symmetry (Fig. 7(b)). This is evident, for the unperturbed C_{4v} case, in its dispersion curves, Fig. 7(c); note that we have plotted around the C_{2v} IBZ to clearly illustrate the correspondence between the two sets of dispersion curves, Figs. 4(b) and 7(c). The additional Dirac cone, for the C_{4v} case, along XM is due to the additional σ_h reflectional symmetry in physical space. Rotating the inclusion set (Fig. 7(a)) results in the breaking of both $\sigma_{h,v}$ symmetries thereby opening up a band-gap (Fig. 7(d)). Importantly, an identical band-gap is present whether we're plotting along the C_{2v} or C_{4v} IBZ's.

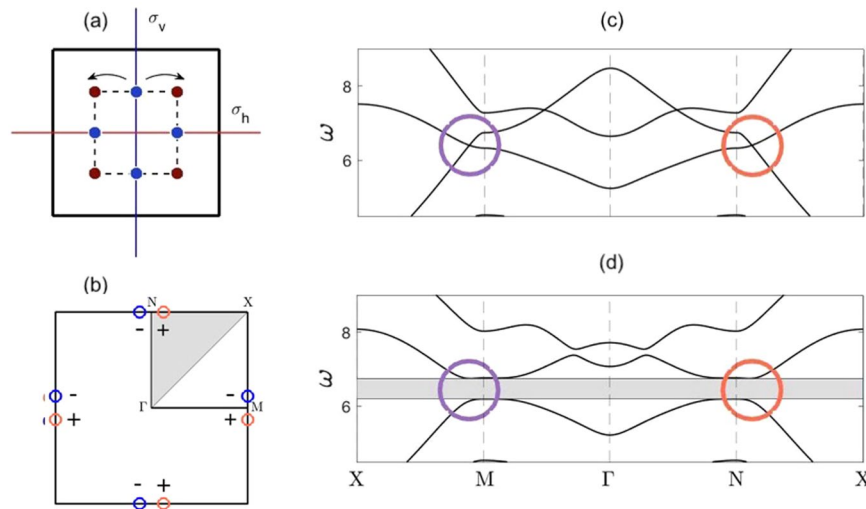


Figure 7. Dispersion curves C_{4v} case — (a) Cellular structure shown; maroon mass value of 1, blue mass value of 2, lattice constant of 2, centroid to vertex mass distance of 0.70. Pre-perturbation structure has σ_v and σ_h symmetries, both of these symmetries are broken in the post-perturbation structure. (b) Shows IBZ (shaded region) within the BZ; circles indicate Dirac cone locations pre-perturbation, whilst \pm denotes $\text{sgn}(C_v)$, post-perturbation. Unlike the C_{2v} case (Fig. 4(b)), Dirac cones now present along both sets of parallel HSLs. (c) Pre-perturbation dispersion curves. We have opted to plot around the IBZ of the C_{2v} case (Fig. 2(b)) in order to explicitly show the Dirac cone that arises from the added σ_h symmetry. (d) Post-perturbation dispersion curves. If we were to plot along the C_{4v} IBZ an identical band-gap, in location and width, would be present.

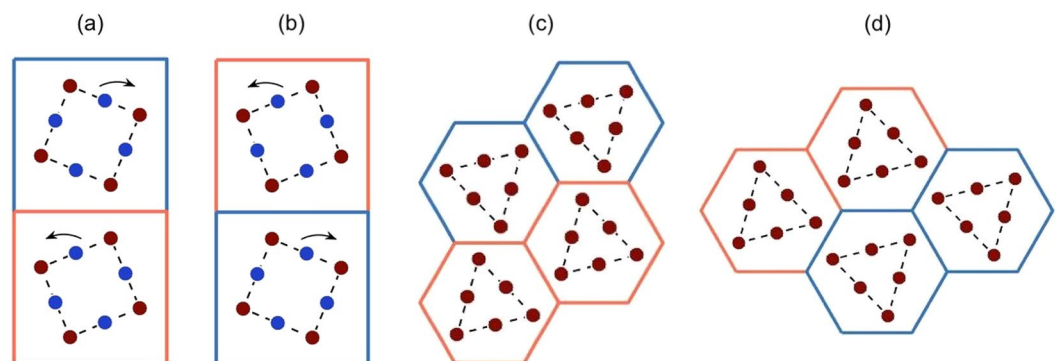


Figure 8. Interface comparison between C_{4v} case (a,b) and graphene-like structure (c,d) — representative hexagonal structure taken from²⁶. Evidently, the two hexagonal zigzag interfaces that host ZLMs are distinct whilst, the two square interfaces, are identical under TRS. Even and odd-parity edge modes exist along the *same* interface for the C_{4v} case and *different* interfaces for the graphene-like structures and C_{2v} cases (Fig. 6(a)). This latter point is what allows for coupling between the pre-bend and post-bend modes, Fig. 10, for the C_{4v} case but not the C_{2v} . Crucially, this property is also what yields three-way splitting for the C_{4v} case, Fig. 1, but *not* for the graphene-like structures.

In the subsequent section, we demonstrate how the additional reflectional symmetry enables mode coupling from the pre-bend to post-bend ZLM thereby allowing for energy navigation around a corner.

Propagation around a bend. A crucial property that allows for wave steering for the C_{4v} case is the presence of Dirac cones along both edges of the BZ. Another important property is that, like the C_{2v} case, both, even and odd edge modes exist, however they are now present along the *same* interface as opposed to different interfaces. The orthogonality of these opposite-parity modes ensures that they do not couple along the same edge. The presence of both parity modes along the same interface (for the C_{4v} case) arises from the relationship between the orange over blue stacking and its reverse (Fig. 8(a,b)). Specifically, it is clearly evident from Fig. 8(a,b) that a right propagating mode for one stacking is a left propagating mode on the other and vice versa. This special property is also what allows for the three-way splitting of energy (see subsection 4.3).

We now move onto deriving an edge mode for the C_{4v} case. Due to there being only a single unique interface, we choose to use a Fourier-Hermite spectral method⁵¹, that purely finds the decaying solution along a single interface, as opposed to simultaneously along both; the latter occurs when the PWE method is used in

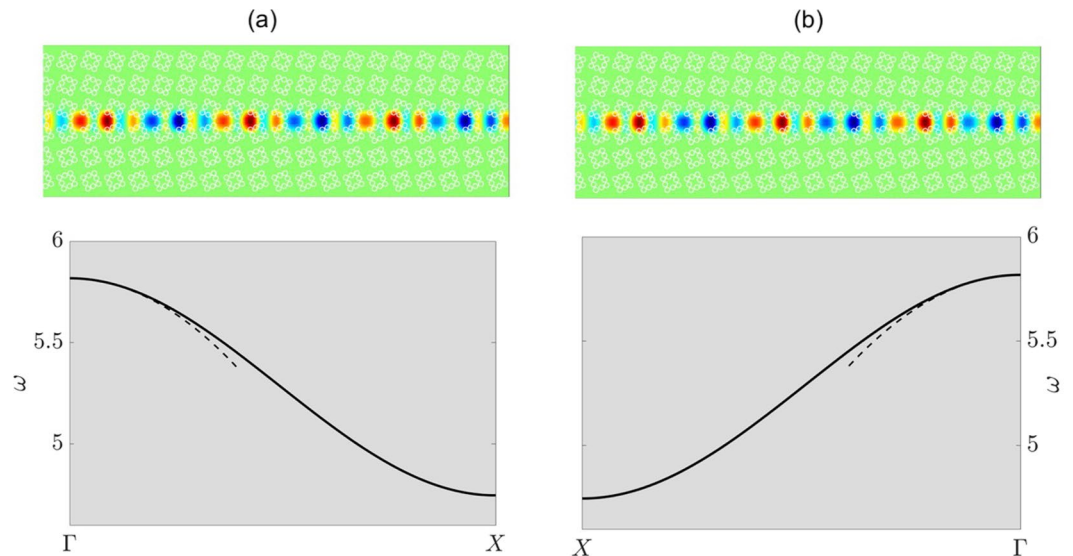


Figure 9. C_{4v} even-parity interfacial mode — *Left* and *right* columns, panels (a,b), pertain to the orange over blue and blue over orange stackings, respectively. Top panels show eigensolutions obtained from Fourier-Hermite method. Bottom panels show that the even-parity interfacial curve, for both stackings, are identical, HFH asymptotics⁵¹ also shown (dashed lines).

conjunction with two-dimensional periodic Bloch conditions. Hence, from Fig. 9, we clearly see that, for a variant of the C_{4v} case, the orange over blue (Fig. 9(a)) or blue over orange (Fig. 9(b)) stacking yields an even-parity decaying mode. More specifically, the orange over blue stacking gives solutions to the right of Γ whilst the blue over orange yields solutions to the left of Γ ; this implies that the two stackings host the same mode and are TRS pairs of each other. Note that a parametric variant of the C_{4v} case was used to ensure faster convergence of the Fourier-Hermite spectral method. The local curvature, and thereby the characterisation of the envelope, is obtained for modes in the vicinity of Γ (see asymptotics in the bottom panels of Fig. 9). Similar to the earlier C_{2v} structure the edge states that arise are topologically nontrivial and gapless²².

Transmission around a bend. The perturbed C_{4v} system has valleys of nonzero C_v along all HSLs of the BZ (Fig. 7(b)). This allows for the strategic arrangement of four structured media such that valleys of opposite $\text{sgn}(C_v)$ overlay each other along, both, horizontal and vertical interfaces, Fig. 10(a). This strategic arrangement necessitates the existence of broadband ZLMs along both of these interfaces simultaneously; therefore, unlike the C_{2v} case, energy is navigable around bends.

The four-cell arrangement shown in Fig. 10(a) encompasses the design of the nodal region (and by extending it outwards, the entire region) for the $\pi/2$ wave steerer and three-way energy-splitter. If the bottom-right inclusion set is rotated clockwise then a wave incident along the leftmost interface will follow the red arrows around the $\pi/2$ bend. The indistinguishable, pre- and post-bend interfaces, ensure that, as the energy traverses the turning point, an even-parity mode will couple into itself. An example of, topological wave steering around a bend, is shown in Fig. 10(b–d). Notably, the $\pi/2$ wave steerers observed within hexagonal structures require coupling between a zigzag mode with an armchair mode. The latter termination hosts topologically *trivial* edge states due to the overlapping regions of identical $\text{sgn}(C_v)$ resulting in gapped states. Contrastingly, the structure shown in Fig. 10(a) allows for topologically *nontrivial* $\pi/2$ wave steering.

Similar to the C_{2v} ZLM, the short-scale oscillations are discernible from the long-scale modulation. The importance of this long-scale modulation is numerically elucidated in the subsequent section.

Relevance of envelope to transmission around a bend. The characterisation of the energy-carrying envelope is important, as the tuning of it can lead to higher transmission along finite length interfaces. This principle is elucidated by examining the wave-steering example, Fig. 10(e,f); using finite element integration the intensity of the wave-field in each arm of such a steerer is calculated. The ratio of these intensities is the measure of the transmission of the wave steerer (Fig. 10(f)); this quantity can be seen to oscillate rapidly across the band-gap. This is similar to the behaviour of conventional Fabry-Pérot resonators, where for maximal transmission an integer number of wavelengths must be completely contained in each lead. Thus the length of the interfaces is of importance for optimising the transmission. This effect is clearly seen by the contrast in transmission between Fig. 10(e) and (b–d). Despite the paradigm utilising the valley-Hall topological phase, the robustness and bandwidth of the effect can be further increased, by parametric variation, introducing a TRS-breaking active component, nonlinearity and/or resonators within the nodal region.

Topological 3-way splitter. We now move onto the construction of the three-way energy-splitter; rotating the bottom-right inclusion set anti-clockwise, in Fig. 10(a); results in four partitions of geometrically distinct media. A wave incoming, from the leftmost interface, will now follow, both, the red and green arrows thereby splitting

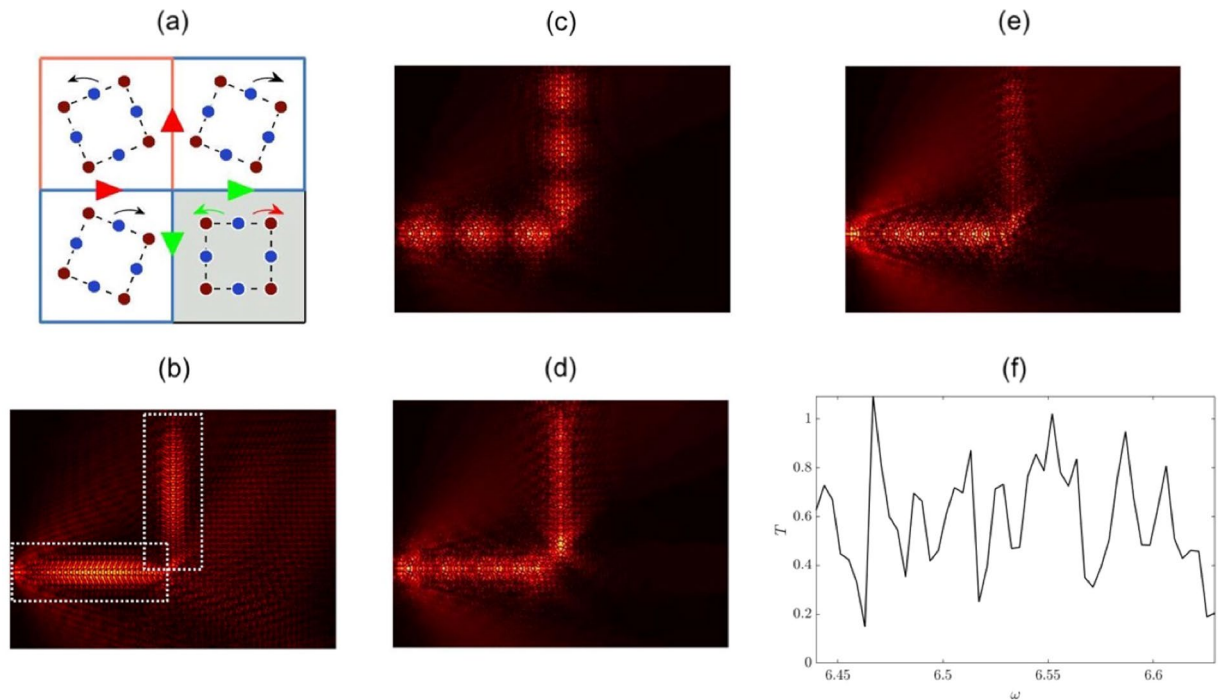


Figure 10. Wave-steering and energy-splitting — (a) By extending this nodal region outwards the entire structured domain for both effects is obtained. If the bottom-right quadrant's inclusion set is rotated rightwards then a left-sided incident ZLM would follow the red arrows around the bend; leading to the modal pattern in the right panel. If the same set of inclusions is rotated leftwards, then energy is partitioned three-ways away from the nodal point, yielding the three-way energy-splitter, Fig. 1. (b) Example of topological wave steering. Similar to C_{2v} ZLM, Fig. 6(b), long-scale modulation is distinguishable from the short-scale oscillations. Wave steering examples — (a,b) Panels show different examples of high-transmission wave steering. Notably, in each of these cases the long-scale envelope is discernible, and more importantly, the wavelengths of these envelopes is entirely contained within the first lead thereby allowing for near-perfect transmission around the bend. (c) Shows an instance where the incident ZLM impacts the turning point with maximum amplitude, resulting in significant backscattering. Right-sided ZLM shows the highly variable transmission of this long-wavelength wave steerer. Transmission is calculated from the ratio of the intensities contained within the two boxes (shown in the upper-left panel). The overlap of the boxes introduces a small numerical error that can yield unphysical transmissions (e.g. $\omega = 6.465$).

the energy three-ways. The resulting scattering solution, for a monopolar source, is shown in Fig. 1; the topological nature of the modes is demonstrated by the chiral fluxes. The three-way splitter can be tuned to a wave steerer by rotating the cellular structures in lower-right quadrant.

For a mode to couple, from one lead to another, the chirality of the modes must match^{16–20,26–39}. For the square C_{4v} case this condition is satisfied due to the relationship between the interfaces Fig. 8(a,b); an incident even mode couples to itself along the three exit leads, Figs. 1 and 11(a). The κ excited for the upper and lower leads (Fig. 1) matches the left lead interface (orange over blue), hence an incident even mode at valley K will couple to itself along the upper and lower leads.

Importantly, the right-sided interface (blue over orange) is the reverse of the left-sided interface, hence a right propagating mode on the right-sided interface is identical to a left propagating mode on the left-sided interface. Mathematically, the latter implies that $\kappa_L = -\kappa_R$ where $\kappa_{L,R}$ are the wavevectors along the left and right-sided interfaces respectively. Due to the chiral relationship between the interfaces the κ_L and κ_R modes conveniently have matching chirality. This allows for the seamless coupling between the left-sided and right-sided modes however there remains a phase difference to account for. In order for the left-sided mode to couple with the right-sided mode a phase must be acquired as the incident wave passes through the nodal point; this is similar to how an incident wave acquires a phase when it passes through a gratings coupler⁵². This phase difference between the modes implies that $\kappa_L + \kappa_R = 0$ thereby resulting in a zero imaginary component along the rightward lead, Fig. 11(b). Despite this phase difference, the chiral relationship between the two interfaces, Fig. 8(a,b), ensures that there is conservation of chirality (a necessary condition for topological mode coupling) throughout this four-region structured domain. The relationship between the interfaces is crucial in allowing the third lead to be triggered. This provides further evidence for why only two-way splitting has thus far been obtained for TRS-breaking topological systems^{53–56}.

Comparing our design with that of a similar hexagonal network, see^{16–20,26–39} and Fig. 11(c), we note that the chirality and/or phase velocity mismatch results in energy being redirected solely along the two vertical partitions

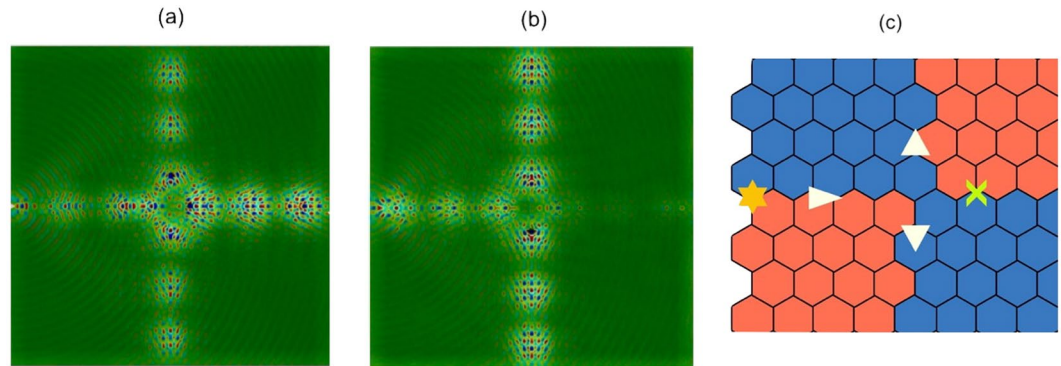


Figure 11. Real (a) and imaginary (b) components of the displacement field shown in Fig. 1. Notably in panel (a), the monopolar source triggers an even-parity ZLM along the left-sided interface; this mode couples into identical parity modes along all three outgoing leads. The absence of excitation along the right-hand lead, in panel (b), indicates that there is a phase difference between this lead and the other three excited leads. Panel (c) Two-way energy-splitting for hexagonal structure and three-way energy-splitting for C_{4v} case — The suppression of intervalley scattering restricts graphene-like structures to two-way splitting of energy. The incoming ZLM, that has group velocity $v_g > 0$ and wavevector $+\kappa$, is unable to couple to the post-nodal region ZLM, $v_g > 0, -\kappa$, due to their differing valley indices.

(Fig. 11(c)). Additionally there is no such relationship between the blue over orange and orange over blue zigzag interfaces, see Fig. 8(c,d). This conservation of chirality and phase velocity, as well as the two distinct interfaces, restricts the hexagonal structures to two-way energy-splitting^{16–20,27–39}. A comprehensive pictorial comparison between the C_{2v} , C_{4v} cases described herein and the, more common, topologically nontrivial and trivial hexagonal examples described in²⁶ is shown in Fig. 12.

Discussion

We have demonstrated how to geometrically engineer the first-ever broadband three-way energy-splitter. This novel paradigm adds a degree of freedom unavailable to all current designs; namely, the hexagonal valley-Hall energy-splitters^{16–20,27–39} and the two-way cavity guide beam-splitters^{57–67}. This design is reliant upon the time-reversal relationship between the interfaces and hence serves as a paradigm for all scalar wave systems: plasmonics, photonics, acoustics, as well as, for vectorial systems such as plane-strain elasticity, surface acoustic waves and Maxwell equation systems. The additional degree of freedom afforded by this three-way energy-splitter, along with latest advancements in topological physics, will inevitably lead to a myriad of highly tunable, broadband and efficient crystalline networks.

Methods

Dispersion curves and scattering solutions. The dispersion curves throughout the article were obtained using a combination of standard spectral methods as well as the Galerkin method. The standard scheme utilised an adaptation of the plane-wave expansion method to determine the eigenstates⁵⁰. Specifically, a doubly periodic Fourier series expansion is employed by applying Floquet-Bloch conditions on opposite sides of the unit cell, resulting in a generalised eigenvalue problem, that is solved for the non-dimensionalised eigenstates presented throughout.

The dispersive behaviour of the edge states is obtained in a similar manner whereby we consider a stretched unit cell centred on the interface between the two media. Floquet-Bloch conditions are applied to both edges of the ribbon and the height of the ribbon is taken such that it is much greater than the decay length of the localised edge states. The relatively slower decay of the C_{4v} edge mode (Fig. 9) required an alternative method; namely, a Galerkin method where the rate of the decay is built into the expansion of the wavefield through scaled orthonormal Hermite functions⁵¹.

The scattering solutions for point forcings are obtained through the solution of a system of linear equations by standard methods^{42,68}. When a forcing is applied we utilise a Green's function approach where the total wavefield is given for P scatterers by

$$\psi_{n\kappa}(\mathbf{x}) = \psi_s(\mathbf{x}) + \sum_{p=1}^P F_p g(\omega_{n\kappa}, |\mathbf{x} - \mathbf{x}_p|). \quad (18)$$

Using the well-known Green's function⁴², $g(\omega_{n\kappa}, \rho) = (i/8\omega_{n\kappa}^2)[H_0(\omega_{n\kappa}\rho) - H_0(i\omega_{n\kappa}\rho)]$, the unknown reaction terms F_m ($m = 1 \dots P$) come from the linear system

$$F_m = M_m \omega_{n\kappa}^2 \left[\psi_s(\mathbf{x}_m) + \sum_{p=1}^P F_p g(\omega_{n\kappa}, |\mathbf{x}_m - \mathbf{x}_p|) \right]. \quad (19)$$

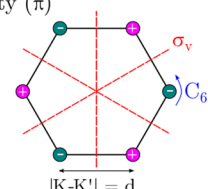
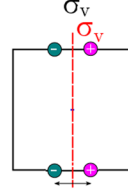
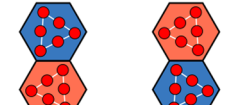
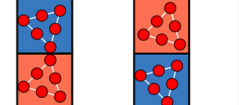
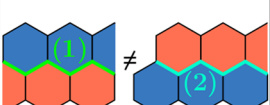
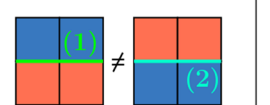
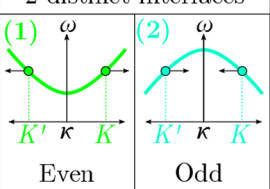
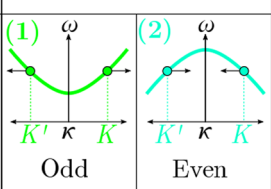
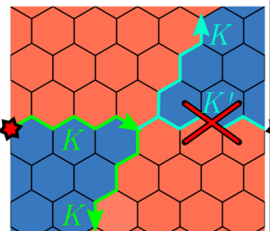
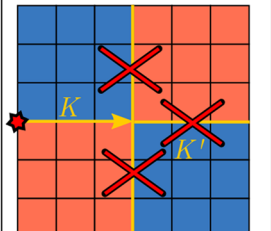
	Hexagon		Square	
Broken Symmetries	$\{\sigma_v\}, C_6, \text{parity } (\pi)$ 			
Berry Curvature Sign (+) (-)	Topologically nontrivial		Topologically trivial	
Edge config.				
Distinct Interfaces				
Edge States:	2 distinct interfaces		1 equivalent interface (modulo TRS)	
Band shape				
Mode parity	Even	Odd	Odd	Even
Coupling				
Pros (+) Cons (-)	<ul style="list-style-type: none"> + Topologically nontrivial + Dirac cones at BZ vertices, hence larger Fourier separation (d) between modes of opposite chirality: enhanced robustness - Only two-way splitting possible without using tunnelling 		<ul style="list-style-type: none"> + Topologically nontrivial - Dirac cones solely located along single set of parallel HSLs, hence only straight-line propagation - Small Fourier separation (d') between modes of opposite chirality 	
	<ul style="list-style-type: none"> + Large Fourier separation between $v_y < 0$ and $v_y > 0$ modes + More than two way splitting possible due to matching phase and group velocity of pre/post-nodal region leads - Topologically trivial, hence no added chiral flux protection 		<ul style="list-style-type: none"> + Topologically nontrivial + Dirac cones along both sets of HSLs hence wave-steering possible + TRS related interfaces yield a 3-way topologically nontrivial energy-splitter - Small Fourier separation (d') between modes of opposite chirality 	

Figure 12. Comparison table between different geometrically engineered states. A topologically nontrivial and trivial example are given for the hexagonal structure²⁶; the two square cases are those included within this article: C_{2v}, C_{4v} .

Characterising energy-carrying envelope and relevance to robustness. The efficacy of transmitting energy around a bend, coupling modes between different leads within a network or even transmission through a straight ZLM is contingent upon the displacement of the mode at the turning, nodal or end point. Knowledge of the long-scale envelope is especially useful for these finite length interfaces as it can be used to minimise the backscattering as one has, in effect, a Fabry-Pérot resonator. Examples of the characterisation of the energy-carrying envelope, using high-frequency homogenisation (HFH)⁵⁰, for the C_{2v} and C_{4v} cases are shown. In addition to this, the interfacial dispersion curves for a variation of the C_{4v} case are derived using a Fourier-Hermite spectral method⁵¹.

To fully characterise the long-scale periodic behaviour of topological edge states along a crystal interface we utilise HFH, applying the methodology directly in reciprocal space⁵¹, to further bolster the plane wave expansion (PWE) method that was used to obtain the dispersion curves. This technique is a multiple scale asymptotic method, that (for non-degenerate curves with locally quadratic curvature) results in the following homogenised PDE,

$$T_{ij} f_{0,X_i X_j} - \omega_0^2 f_0 = 0, \quad (20)$$

where f_0 is the long-scale envelope defined on the coordinate system (X_i, X_j) ; whilst the T_{ij} coefficients fully encapsulates the short-scale behaviour (similar analysis can be carried over to any scalar and vectorial system^{51,69–73}). The tensor coefficients T_{ij} are geometrically dependant and, from the simple solution of the homogenised PDE, determine the envelope wavelength for a given frequency. These coefficients are determined entirely from integrated quantities of the wave-field in physical space. To avoid the need for regularisation (higher order corrections) we work in reciprocal space and calculate the T_{ij} 's directly, using the PWE method. Our eigenvalue problem is recast into matrix form,

$$[\mathbf{A}(\kappa) - \omega^2 \mathbf{B}(\kappa)] \mathbf{W} = 0, \quad (21)$$

with the matrices \mathbf{A} , \mathbf{B} encoding the geometry and forcing of the mass loading.

Expanding in the vicinity of a high symmetry point leads to the following ansatz;

$$\begin{aligned} \omega^2 &= \omega_0^2 + \varepsilon \omega_1^2 + \varepsilon^2 \omega_2^2 + \mathcal{O}(\varepsilon^3), \\ \mathbf{W} &= \mathbf{W}_0 + \varepsilon \mathbf{W}_1 + \varepsilon^2 \mathbf{W}_2 + \mathcal{O}(\varepsilon^3), \\ \mathbf{A} &= \mathbf{A}_0 + \varepsilon \sum_i \kappa_i \underbrace{\frac{\partial \mathbf{A}}{\partial \kappa_i}}_{\mathbf{A}_i^{(1)}} + \varepsilon^2 \sum_{i,j} \kappa_i \underbrace{\frac{\partial^2 \mathbf{A}}{\partial \kappa_i \partial \kappa_j}}_{\mathbf{A}_{ij}^{(2)}} \kappa_j + \mathcal{O}(\varepsilon^3), \end{aligned}$$

with a similar expansion for $\mathbf{B}(\kappa)$. Applying suitable solvability conditions and imposing Bloch conditions on the microscale results in the following tensor coefficients T_{ij} ,

$$\begin{aligned} (\widetilde{\mathbf{W}}_1)_i &\equiv \frac{(\mathbf{W}_1)_i}{\kappa_i} \\ &= - [\mathbf{A}_0 - \omega_0^2 \mathbf{B}_0]^+ (\mathbf{A}_i^{(1)} - \omega_0^2 \mathbf{B}_i^{(1)}) \mathbf{W}_0 T_{ij} \\ &= \frac{\mathbf{W}_0^\dagger (\mathbf{A}_i^{(1)} - \omega_0^2 \mathbf{B}_i^{(1)}) (\widetilde{\mathbf{W}}_1)_i + \frac{1}{2} \mathbf{W}_0^\dagger (\mathbf{A}_{ij}^{(2)} - \omega_0^2 \mathbf{B}_{ij}^{(2)}) \mathbf{W}_0}{\mathbf{W}_0^\dagger \mathbf{B}_0 \mathbf{W}_0}, \end{aligned} \quad (22)$$

where ω_0 and \mathbf{W}_0 are the solutions obtained from the PWE method, and $[\dots]^+$ denotes the pseudoinverse. The explicit characterisation of the envelope is shown in Fig. 6(c).

Received: 20 May 2019; Accepted: 28 November 2019;

Published online: 12 December 2019

References

- Mekis, A. *et al.* High Transmission through Sharp Bends in Photonic Crystal Waveguides. *Physical Review Letters* **77**, 3787–3790, <https://doi.org/10.1103/PhysRevLett.77.3787> (1996).
- Yariv, A., Xu, Y., Lee, R. K. & Scherer, A. Coupled-resonator optical waveguide: a proposal and analysis. *Optics Letters* **24**, 711, <https://doi.org/10.1364/OL.24.000711> (1999).
- Chutinan, A., Okano, M. & Noda, S. Wider bandwidth with high transmission through waveguide bends in two-dimensional photonic crystal slabs. *Appl. Phys. Lett.* **80**, 1698–1700, <https://doi.org/10.1063/1.1458529> (2002).
- Quirrenbach, A. Optical interferometry. *Annu. Rev. Astron. Astrophys.* **39**, 353–401 (2001).
- Kok, P. *et al.* Linear optical quantum computing with photonic qubits. *Annu. Rev. Astron. Astrophys.* **79**, 135 (2007).
- Ju, L. *et al.* Topological valley transport at bilayer graphene domain walls. *Nature* **520**, 650–655 (2015).
- Liu, T., Zakharian, A., Fallahi, M., Moloney, J. & Mansuripur, M. Multimode Interference-Based Photonic Crystal Waveguide Power Splitter. *J. Lightwave Tech.* **22**, 2842–2846, <https://doi.org/10.1109/JLT.2004.834479> (2004).
- Ma, T., Khanikaev, A. B., Mousavi, S. H. & Shvets, G. Guiding Electromagnetic Waves around Sharp Corners: Topologically Protected Photonic Transport in Metawaveguides. *Physical Review Letters* **114** (2015).
- Kane, C. L. & Mele, E. J. Z2 Topological Order and the Quantum Spin Hall Effect. *Phys. Rev. Lett.* **95**, 146802 (2005).
- Xiao, D., Yao, W. & Niu, Q. Valley-Contrasting Physics in Graphene: Magnetic Moment and Topological Transport. *Phys. Rev. Lett.* **99**, 236809 (2007).
- Gao, Z. *et al.* Valley surface-wave photonic crystal and its bulk/edge transport. *Physical Review B* **96**, <https://doi.org/10.1103/PhysRevB.96.201402> (2017).
- Lu, J. *et al.* Observation of topological valley transport of sound in sonic crystals. *Nature Physics* **13**, 369–374 (2016).
- Shalaev, M. I., Walasik, W., Tsukernik, A., Xu, Y. & Litchinitser, N. M. Experimental demonstration of valley-Hall topological photonic crystal at telecommunication wavelengths. *arXiv:1712.07284 [physics]* (2017).
- Ma, T. & Shvets, G. All-Si Valley-Hall Photonic Topological Insulator. *New J. Phys.* **18**, 025012 (2016).
- Makwana, M. P. & Craster, R. V. Geometrically navigating topological plate modes around gentle and sharp bends. *Physical Review B* **98**, <https://doi.org/10.1103/PhysRevB.98.184105> (2018).
- Cheng, X. *et al.* Robust reconfigurable electromagnetic pathways within a photonic topological insulator. *Nat. Mat.* **15**, 4573 (2016).

17. Wu, X. *et al.* Direct observation of valley-polarized topological edge states in designer surface plasmon crystals. *Nature Communications* **8**, <https://doi.org/10.1038/s41467-017-01515-2> (2017).
18. Xia, B.-Z. *et al.* Topological phononic insulator with robust pseudospin-dependent transport. *Phys. Rev. B* **96**, <https://doi.org/10.1103/PhysRevB.96.094106> (2017).
19. Zhang, L. *et al.* Manipulation of valley-polarized topological kink states in ultrathin substrate-integrated photonic circuitry. *arXiv:1805.03954v2* 15 (2018).
20. Qiao, Z., Jung, J., Niu, Q. & MacDonald, A. H. Electronic highways in bilayer graphene. *Nano Lett.* **11**, 3453–3459 (2011).
21. He, W.-Y. & Chan, C. T. The emergence of Dirac points in photonic crystals with mirror symmetry. *Sci. Reports* **5**, 8186 (2015).
22. Xia, B.-Z. *et al.* Observation of valleylike edge states of sound at a momentum away from the high-symmetry points. *Physical Review B* **97**, 155124, <https://doi.org/10.1103/PhysRevB.97.155124> (2018).
23. Chen, J.-H., Cullen, W. G., Jang, C., Fuhrer, M. S. & Williams, E. D. Defect Scattering in Graphene. *Physical Review Letters* **102**, <https://doi.org/10.1103/PhysRevLett.102.236805> (2009).
24. Morozov, S. V. *et al.* Strong Suppression of Weak Localization in Graphene. *Physical Review Letters* **97**, <https://doi.org/10.1103/PhysRevLett.97.016801> (2006).
25. Morpurgo, A. F. & Guinea, F. Intervalley Scattering, Long-Range Disorder, and Effective Time-Reversal Symmetry Breaking in Graphene. *Physical Review Letters* **97**, <https://doi.org/10.1103/PhysRevLett.97.196804> (2006).
26. Makwana, M. & Craster, R. Designing topological energy-splitters and valley networks in two-dimensional crystals. *Physical Review B* (2018).
27. Cha, J., Kim, K. W. & Daraio, C. Experimental realization of on-chip topological nanoelectromechanical metamaterials. *Nature* **564**, 229–233, <https://doi.org/10.1038/s41586-018-0764-0> (2018).
28. He, C. *et al.* Acoustic topological insulator and robust one-way transport. *Nature Physics* **12**, 3867 (2016).
29. He, X.-T. *et al.* A Silicon-on-Insulator Slab for Topological Valley Transport. *arXiv* 1805.10962 (2018).
30. He, M., Zhang, L. & Wang, H. Two-dimensional photonic crystal with ring degeneracy and its topological protected edge states. *Scientific Reports* **9**, <https://doi.org/10.1038/s41598-019-40677-5> (2019).
31. Khanikaev, A. B. & Shvets, G. Two-dimensional topological photonics. *Nat. Photonics* **11**, 763–773, <https://doi.org/10.1038/s41566-017-0048-5> (2017).
32. Nanthakumar, S. *et al.* Inverse design of quantum spin hall-based phononic topological insulators. *Journal of the Mechanics and Physics of Solids* **125**, 550–571, <https://doi.org/10.1016/j.jmps.2019.01.009> (2019).
33. Ozawa, T. *et al.* Topological Photonics. *Reviews of Modern Physics* **91**, <https://doi.org/10.1103/RevModPhys.91.015006>, ArXiv:1802.04173 (2019).
34. Qiao, Z. *et al.* Current partition at topological channel intersections. *Phys. Rev. Lett.* **112**, 206601 (2014).
35. Schomerus, H. Helical scattering and valleytronics in bilayer graphene. *Physical Review B* **82**, <https://doi.org/10.1103/PhysRevB.82.165409> (2010).
36. Shen, Y. *et al.* Valley-projected edge modes observed in underwater sonic crystals. *Applied Physics Letters* **114**, 023501, <https://doi.org/10.1063/1.5049856> (2019).
37. Xia, B., Fan, H. & Liu, T. Topologically protected edge states of phoxonic crystals. *International Journal of Mechanical Sciences* **155**, 197–205, <https://doi.org/10.1016/j.ijmecsci.2019.02.037> (2019).
38. Yan, M. *et al.* On-chip valley topological materials for elastic wave manipulation. *Nature Materials* **17**, 993–998, <https://doi.org/10.1038/s41563-018-0191-5> (2018).
39. Ye, L. *et al.* Observation of acoustic valley vortex states and valley-chirality locked beam splitting. *Physical Review B* **95**, <https://doi.org/10.1103/PhysRevB.95.174106> (2017).
40. Hou, T. *et al.* Metallic Network of Topological Domain Walls. *arXiv:1904.12826 [cond-mat]*, ArXiv: 1904.12826 (2019).
41. Landau, L. D. & Lifshitz, E. M. *Theory of elasticity*, 2nd edn. (Pergamon Press, 1970).
42. Evans, D. V. & Porter, R. Penetration of flexural waves through a periodically constrained thin elastic plate floating in it vacuo and floating on water. *J. Engng. Math.* **58**, 317–337 (2007).
43. Xia, B., Wang, G. & Zheng, S. Robust edge states of planar phononic crystals beyond high-symmetry points of Brillouin zones. *Journal of the Mechanics and Physics of Solids* **124**, 471–488, <https://doi.org/10.1016/j.jmps.2018.11.001> (2019).
44. Dresselhaus, M. S., Dresselhaus, G. & Jorio, A. *Group theory: application to the physics of condensed matter* (Springer-Verlag, 2008).
45. Heine, V. *Group Theory in Quantum Mechanics: An Introduction to Its Present Usage* (Dover Publications).
46. Bostan, C. *Design and fabrication of quasi-2D photonic crystal components based on silicon-on-insulator technology*. PhD Thesis, s.n.], S.I. (2005).
47. Ochiai, T. Photonic realization of the (2+1)-dimensional parity anomaly. *Phys. Rev. B* **86** (2012).
48. Fefferman, C. L., Lee-Thorp, J. P. & Weinstein, M. I. Bifurcations of edge states—topologically protected and non-protected—in continuous 2d honeycomb structures. *2D Materials* **3**, 014008, <https://doi.org/10.1088/2053-1583/3/1/014008> (2016).
49. Qian, K., Apigo, D. J., Prodan, C., Barlas, Y. & Prodan, E. Theory and Experimental Investigation of the Quantum Valley Hall Effect. *arXiv:1803.08781 [cond-mat]* (2018).
50. Makwana, M., Antonakakis, T., Maling, B., Guenneau, S. & Craster, R. V. Wave Mechanics in Media Pinned at Bravais Lattice Points. *SIAM Journal on Applied Mathematics* **76**, 1–26, <https://doi.org/10.1137/15M1020976> (2016).
51. Chaplain, G. J., Makwana, M. P. & Craster, R. V. Rayleigh-Bloch, topological edge and interface waves for structured elastic plates. *arXiv:1812.07531 [physics]* (2018).
52. Chuang, S. L. *Physics of Photonic Devices* (2009).
53. Hammer, R. & Pötzt, W. Dynamics of domain-wall Dirac fermions on a topological insulator: A chiral fermion beam splitter. *Physical Review B* **88**, <https://doi.org/10.1103/PhysRevB.88.235119> (2013).
54. Hammer, R., Ertler, C. & Pötzt, W. Solitonic Dirac fermion wave guide networks on topological insulator surfaces. *Applied Physics Letters* **102**, 193514, <https://doi.org/10.1063/1.4807012> (2013).
55. Wang, X. S., Su, Y. & Wang, X. R. Topologically protected unidirectional edge spin waves and beam splitter. *Physical Review B* **95**, <https://doi.org/10.1103/PhysRevB.95.014435> (2017).
56. Wang, X., Zhang, H. & Wang, X. Topological Magnonics: A Paradigm for Spin-Wave Manipulation and Device Design. *Physical Review Applied* **9**, <https://doi.org/10.1103/PhysRevApplied.9.024029> (2018).
57. Zhao, D., Zhang, J., Yao, P., Jiang, X. & Chen, X. Photonic crystal Mach-Zehnder interferometer based on self-collimation. *Applied Physics Letters* **90**, 231114, <https://doi.org/10.1063/1.2746942> (2007).
58. Pustai, D. M., Shi, S., Chen, C., Sharkawy, A. & Prather, D. W. Analysis of splitters for self-collimated beams in planar photonic crystals. *Optics Express* **12**, 1823, <https://doi.org/10.1364/OPEX.12.001823> (2004).
59. Tang, Y. *et al.* One-way Acoustic Beam Splitter. *Scientific Reports* **8**, 13573 (2018).
60. Prather, D. W. *et al.* Self-collimation in photonic crystal structures: a new paradigm for applications and device development. *Journal of Physics D: Applied Physics* **40**, 2635 (2007).
61. Shi, S., Sharkawy, A., Chen, C., Pustai, D. M. & Prather, D. W. Dispersion-based beam splitter in photonic crystals. *Optics Letters* **29**, 617, <https://doi.org/10.1364/OL.29.000617> (2004).
62. Luan, P.-G. & Chang, K.-D. Periodic dielectric waveguide beam splitter based on co-directional coupling. *Optics Express* **15**, 4536, <https://doi.org/10.1364/OE.15.004536> (2007).

63. Liu, X. *et al.* Multiple wavelength-selecting and beam-splitting photonic crystal functional device based on the mode coupling between the central microcavity and the adjacent waveguides. *Applied Optics* **57**, 5405, <https://doi.org/10.1364/AO.57.005405> (2018).
64. Fan, S.-H., Johnson, S. G., Joannopoulos, J. D., Manoatou, G. & Haus, H. A. Waveguide branches in photonic crystals. *J. Opt. Soc. Am. B* **18**, 162–165 (2001).
65. Bostan, C. & de Ridder, R. Design of waveguides, bends and splitters in photonic crystal slabs with hexagonal holes in a triangular lattice. In *Proceedings of 2005 7th International Conference Transparent Optical Networks, 2005*, vol. 1, 130–135, <https://doi.org/10.1109/ICTON.2005.1505768> (IEEE, Barcelona, Catalonia, Spain, 2005).
66. Boscolo, S., Midrio, M. & Krauss, T. F. Y junctions in photonic crystal channel waveguides: high transmission and impedance matching. *Optics Letters* **27**, 1001, <https://doi.org/10.1364/OL.27.001001> (2002).
67. Bayindir, M., Temelkuran, B. & Ozbay, E. Photonic-crystal-based beam splitters. *Applied Physics Letters* **77**, 3902–3904, <https://doi.org/10.1063/1.1332821> (2000).
68. Torrent, D., Mayou, D. & Sanchez-Dehesa, J. Elastic analog of graphene: Dirac cones and edge states for flexural waves in thin plates. *Phys. Rev. B* **87**, 115143 (2013).
69. Antonakakis, T. & Craster, R. V. High frequency asymptotics for microstructured thin elastic plates and platonics. *Proc. R. Soc. Lond. A* **468**, 1408–1427 (2012).
70. Antonakakis, T., Craster, R. V. & Guenneau, S. Asymptotics for metamaterials and photonic crystals. *Proc. R. Soc. Lond. A* **469**, 20120533 (2013).
71. Antonakakis, T., Craster, R. V. & Guenneau, S. Homogenization for elastic photonic crystals and metamaterials. *J. Mech. Phys. Solids* **71**, 84–96 (2014).
72. Craster, R. V., Kaplunov, J., Nolde, E. & Guenneau, S. High frequency homogenization for checkerboard structures: Defect modes, ultra-refraction and all-angle-negative refraction. *J. Opt. Soc. Amer. A* **28**, 1032–1041 (2011).
73. Craster, R. V., Kaplunov, J. & Pichugin, A. V. High frequency homogenization for periodic media. *Proc R Soc Lond A* **466**, 2341–2362 (2010).

Acknowledgements

Both authors thank the EPSRC for their support through Grant No. EP/L024926/1 as well as Richard. V. Craster. The authors also thank the referees for their constructive and insightful comments.

Author contributions

M.P.M. conceived the idea, did the majority of the theory, numerical simulations and write-up. G.C. did the numerical simulations shown in Figures 1(c) and 6(c) (envelope component), 9, 10(f). The underlying theory for these components, as well as the illustrative table Fig. 12 were also done by G.C.

Competing interests

The authors declare no competing interests.

Additional information

Correspondence and requests for materials should be addressed to M.P.M.

Reprints and permissions information is available at www.nature.com/reprints.

Publisher's note Springer Nature remains neutral with regard to jurisdictional claims in published maps and institutional affiliations.



Open Access This article is licensed under a Creative Commons Attribution 4.0 International License, which permits use, sharing, adaptation, distribution and reproduction in any medium or format, as long as you give appropriate credit to the original author(s) and the source, provide a link to the Creative Commons license, and indicate if changes were made. The images or other third party material in this article are included in the article's Creative Commons license, unless indicated otherwise in a credit line to the material. If material is not included in the article's Creative Commons license and your intended use is not permitted by statutory regulation or exceeds the permitted use, you will need to obtain permission directly from the copyright holder. To view a copy of this license, visit <http://creativecommons.org/licenses/by/4.0/>.

© The Author(s) 2019